



OPEN

# Laser-induced Greenish-Blue Photoluminescence of Mesoporous Silicon Nanowires

SUBJECT AREAS:

NANOWIRES

NANOSCALE MATERIALS

Received

29 January 2014

Accepted

9 April 2014

Published

13 May 2014

Yan-Ru Choi<sup>1\*</sup>, Minrui Zheng<sup>2\*</sup>, Fan Bai<sup>3\*</sup>, Junjun Liu<sup>3</sup>, Eng-Soon Tok<sup>2</sup>, Zhifeng Huang<sup>3,4</sup>  
& Chorng-Haur Sow<sup>2</sup>

<sup>1</sup>Hwa Chong Institution, 661 Bukit Timah Rd., Singapore 269734, Singapore, <sup>2</sup>Department of Physics, 2 Science Drive 3, National University of Singapore (NUS), Singapore 117542, Singapore, <sup>3</sup>Department of Physics, Institute of Advanced Materials, Partner State Key Laboratory of Environmental and Biological Analysis, Hong Kong Baptist University (HKBU), Kowloon Tong, Hong Kong SAR, P. R. China, <sup>4</sup>HKBU Institute of Research and Continuing Education, A21 1, Virtual University Park Building, South Area Hi-Tech Industrial Park, Shenzhen, Guangdong Province, P. R. China.

Correspondence and requests for materials should be addressed to Z.F.H. (zhuang@hkbu.edu.hk) or C.H.S. (physowch@nus.edu.sg)

\* These authors contributed equally to this work.

**Solid silicon nanowires and their luminescent properties have been widely studied, but lesser is known about the optical properties of mesoporous silicon nanowires (mp-SiNWs). In this work, we present a facile method to generate greenish-blue photoluminescence (GB-PL) by fast scanning a focused green laser beam (wavelength of 532 nm) on a close-packed array of mp-SiNWs to carry out photo-induced chemical modification. The threshold of laser power is 5 mW to excite the GB-PL, whose intensity increases with laser power in the range of 5–105 mW. The quenching of GB-PL comes to occur beyond 105 mW. The in-vacuum annealing effectively excites the GB-PL in the pristine mp-SiNWs and enhances the GB-PL of the laser-modified mp-SiNWs. A complex model of the laser-induced surface modification is proposed to account for the laser-power and post-annealing effect. Moreover, the fast scanning of focused laser beam enables us to locally tailor mp-SiNWs en route to a wide variety of micropatterns with different optical functionality, and we demonstrate the feasibility in the application of creating hidden images.**

The development of highly integrated optoelectronic circuits tends to impose a wide diversity of functions onto the silicon-based electrical components, including lasers<sup>1,2</sup>, waveguides<sup>3</sup>, light emitting diodes<sup>4,5</sup>, photovoltaic<sup>6–9</sup>, and bio-imaging<sup>10</sup>. Optoelectronic functions substantially require sufficient optical absorption, in conflict with the indirect band gap and momentum reservation via phonon-assisted relaxation in silicon<sup>11,12</sup>. When shrinking silicon comparable to or below the bulk exciton Bohr radius of  $\sim 4$  nm<sup>13</sup>, it has been proposed that quantum confinement (QC) tends to increase the band gap and tune it from indirect to direct, resulting in an enhancement of optical absorption<sup>14,15</sup>. One shrinking approach is to reduce silicon nanoparticles by surface oxidation and subsequent removal of shell silica, producing PL engineerable over the full visible spectrum (from red color with a diameter of  $\sim 3$  nm to blue with  $\sim 1$  nm)<sup>16,17</sup>. Another method is to porosify silicon either by electrochemical anodization to create porous silicon made of interconnected matrixes of nanocrystalline silicon skeletons<sup>18</sup>, or by metal-assisted chemical etching (MACE)<sup>19</sup> to generate mp-SiNWs<sup>20,21</sup>.

PL denotes light emission under photon excitation, playing a significant role in optoelectronics. Since 1990's the PL of porous silicon has been widely studied<sup>22</sup>, reporting that porous silicon can emit blue (wavelength  $\lambda$  of 400–500 nm)<sup>23–25</sup>, blue-green ( $\lambda$  centered at 490 nm)<sup>26</sup>, red (560–860 nm)<sup>27–29</sup> and infrared (900–2000 nm) light<sup>30–32</sup>. However, the mechanism is under debate mainly among four models, including QC, surface states, defects in oxides and specific chemical species<sup>33</sup>. As one-dimensional porous silicon, mp-SiNWs can be created by MACE<sup>34</sup>, and tend to attract increasing fundamental and technical attentions<sup>35–40</sup>. It was reported that mp-SiNWs emit red PL centered at  $\sim 650$  nm, ascribed to deep QC and/or surface/defect states<sup>20,21</sup>. The red PL shows a shift in intensity and center  $\lambda$  with ambient temperature, attributed to either multiple-level transition<sup>41</sup> or a combined effect of temperature-assisted anti-trapping below 160 K and thermal quenching at 160–300 K<sup>42</sup>. The NW porosity is determined by the MACE conditions, and increases with the doping level of as-etched silicon wafers, concentration of etchants (e.g. H<sub>2</sub>O<sub>2</sub>), temperature and etching duration. For instance, when H<sub>2</sub>O<sub>2</sub> increases from 0.05 to 0.2 mol/L, the porosity rises from  $<47\%$  to 66%, resulting in red shift of PL from 450 nm to 540 nm<sup>40</sup>. A raise in the doping level of n-Si(100) also causes red shift from 560 nm<sup>43</sup> to 650 nm<sup>20</sup>. On the contrary, QC predicts a blue shift with an increase of porosity<sup>44</sup>. Lin *et al.* decomposed a broad PL peak into two centered at 750 nm and 850 nm<sup>45</sup>. The first peak was ascribed to the red-excitons localized at the Si/SiO<sub>x</sub> interfaces, and the



second to the triplet-singlet transition related to the Si-H surface states<sup>46</sup>. Analogous to porous silicon, it is still ambiguous how mp-SiNWs emit light under photon excitation.

In this work, a facile method is presented to locally modify PL of mp-SiNWs by scanning a focused laser beam rapidly onto an array of close-packed mp-SiNWs. The laser scanning quenches and slightly redshifts the red PL of pristine mp-SiNWs, and generates greenish-blue (GB) PL. The intensity of GB-PL is engineered with laser power and post-laser annealing. Spectral characterizations are systematically carried out to study the laser-induced modification, and probe the origin of GB-PL. Furthermore, we make use of this technique to create a wide variety of micro-patterns with controllable optical functionality. This can provide greater building blocks for photoelectronics and other potential applications, e.g. creating hidden features. To the best of our knowledge, this is the first report on tuning PL of mp-SiNWs by focused laser beam with micro-scale spatial resolution.

## Results

**Laser-induced greenish-blue PL of mp-SiNWs.** MACE was carried out to create an array of close-packed mp-SiNWs homogeneously grown on a Si wafer in an area of  $1.5 \times 1.5 \text{ cm}^2$ . The as-grown mp-SiNWs were subjected to the micro-patterning and micro-modification using a typical optical microscope system that was coupled with an external laser beam. Fig. 1 shows a schematic diagram of the focused laser beam setup used in this work, and the setup details are described in the experimental section. Parallel beam from a diode laser was directed into an upright optical microscope via two reflecting mirrors. Inside the microscope, the beam was directed towards an objective lens via a dichroic filter, and then focused on a sample by an objective lens. The sample was placed on a computer-controlled, motorized stage. By moving the sample stage in a programmable manner with respect to the focused beam, it is able to create a wide variety of micropatterns on substrates. The same objective lens was used to collect light reflected from the sample for viewing. A CCD camera was used to capture the images of laser trimming processes, so as to inspect the created structures simultaneously through a TV monitor.

The fast laser scanning was carried out in ambient conditions, and micro-patterns were constructed on the mp-SiNW arrays. When the

laser beam is focused upon the mp-SiNWs, the absorbed laser energy may give rise to changes in the physical properties of mp-SiNWs, e.g. notably in fluorescence. Fig. 2a–b show two fluorescence microscopy (FM) images of micropatterns created with a laser power of 57.8 mW on the as-grown mp-SiNW arrays, under the UV (330–385 nm) excitation. FM shows that the as-grown and laser-treated mp-SiNWs appear to be reddish and GB in color, respectively. The features in the micropatterns are well defined by the focused laser beam, and the boundaries between the as-grown and laser-modified regions can be clearly identified. The spatial resolution depends on the size of focused laser spot and laser power. Fig. 2c shows that the pristine mp-SiNWs have a PL peak centered at  $\sim 750 \text{ nm}$ , accounting for the reddish FM. The focused laser treatment quenches the reddish PL peak and make it slightly redshift, and distinctly creates a new peak centered at  $\sim 550 \text{ nm}$ , consistent with the GB-FM.

*The dependence on laser power.* In ambient conditions, micro-box patterns were created by the fast laser scanning of as-grown mp-SiNW arrays with laser power in the range of 0–142 mW (Fig. 3a), illuminating that the threshold to generate the GB fluorescence is  $\sim 5 \text{ mW}$  (Fig. 3a-iii). Fig. 3b shows the corresponding PL spectra of these micro-boxes, representing that the reddish PL is gradually suppressed with laser power before reaching the threshold, followed by a red shift and quenching beyond the power threshold. At a laser power above 18 mW, the GB-PL centered at 530 nm clearly shows up. No detection of the GB-PL at 5.3 mW may be attributed to insufficient detection sensitivity in PL. We integrated the intensity of PL spectra in 400–600 nm (Fig. 3b), and made a plot of the integrated PL intensity versus laser power in Fig. 3c. It is illuminated in Fig. 3c that beyond the threshold the GB-PL intensity generally increases with laser power in the range of 5–105 mW, though there is a slight reduction from 58 to 73 mW. Above 105 mW, the GB-PL tends to be quenched.

*The post-laser annealing effect.* The GB-PL can be enhanced by the post-laser annealing. Fig. 4a shows a FM image of a microbox created at a laser power of  $\sim 73 \text{ mW}$ . Then the sample was annealed at  $300^\circ\text{C}$  for 1 hour, in vacuum of  $10^{-2} \text{ Torr}$ . The post-laser annealing causes a significant increase in the intensity of GB fluorescence (Fig. 4b), clearly illustrated by the PL spectra in Fig. 4c. Meanwhile, the fluor-

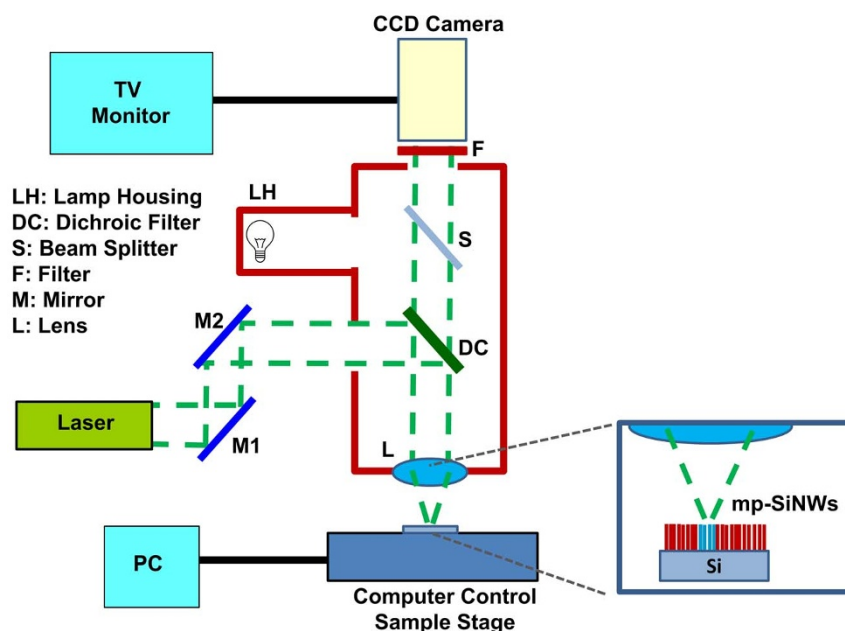


**Figure 1** | Schematic of the optical microscope-focused laser beam set-up for micro-patterning. The box illustrates a zoom-in view of the laser modification on a mp-SiNW array in ambient conditions.

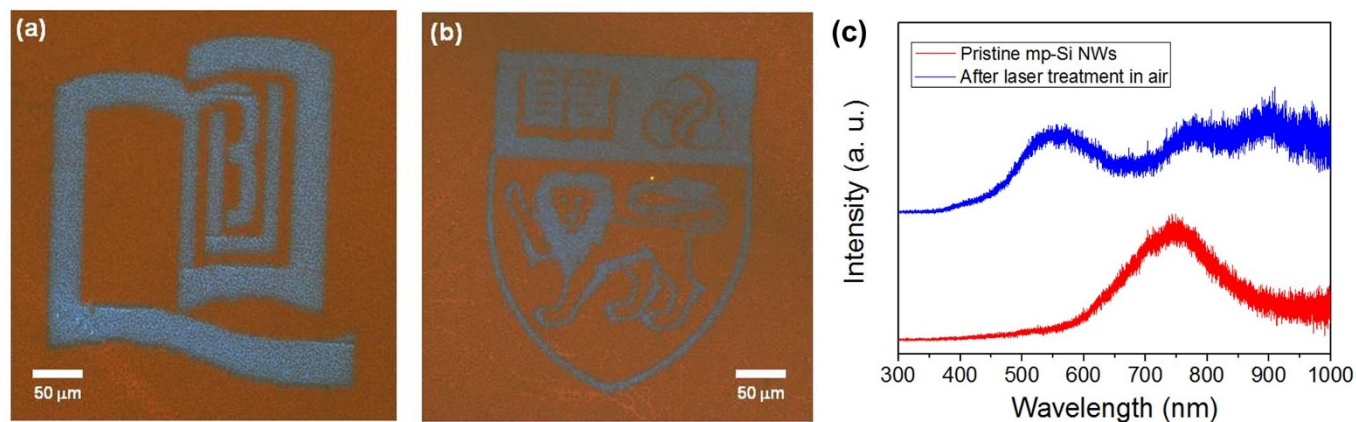


**Figure 2** | (a, b) FM images of micropatterns created by scanning the focused laser beam on mp-SiNW arrays. (c) PL spectra of the as-grown and laser-modified mp-SiNWs. The laser power was  $\sim 58$  mW.

escence of the pristine mp-SiNWs turns from reddish to dark blue, ascribed to the generation of a small hump in the GB region (500–600 nm, Fig. 4d). The annealing also makes the reddish PL redshift slightly.

**Mechanism of the laser-induced GB-PL.** *Laser-induced oxidation of mp-SiNWs (at a laser power of 55–105 mW).* First of all, the laser-induced change in the morphology of mp-SiNWs was studied by SEM and TEM. SEM barely shows any significant laser-induced change in the mp-SiNW morphology (Fig. 5a versus 5b, and 5c versus 5d). Upon closer inspection in Fig. 5d, the laser-treated mp-SiNWs appear to be “rounded” and “fused” together. The “rounded” features may stem from that high-power scanning of focused laser gives rise to rapid heating which partially melts mp-SiNWs; when the

laser moves away, local heat rapidly dissipates leading to re-solidification of the melted sections. The intense local heating may promote local oxidation and create surface defects in mp-SiNWs. TEM clearly shows that the laser irradiation at  $\sim 55$  mW significantly reduces the porosity of mp-SiNWs (Fig. 5e vs 5f), probably ascribed to the laser-induced oxidation which facilitates oxygen diffusion into the interfacial  $\text{SiO}_x$  layers. Fig. 5g clearly shows that the fast laser scanning does generate a thick layer of  $\text{SiO}_x$  in mp-SiNWs, and Fig. 5h illustrates that locally amorphous  $\text{SiO}_x$  induced by the laser oxidation completely surround the shrunk single crystalline Si skeletons.

Spectral characterizations were systematically carried out to demonstrate the laser-induced oxidation. Firstly, SEM-EDS shows that the pristine mp-SiNWs have atomic oxygen percentage (O%) of

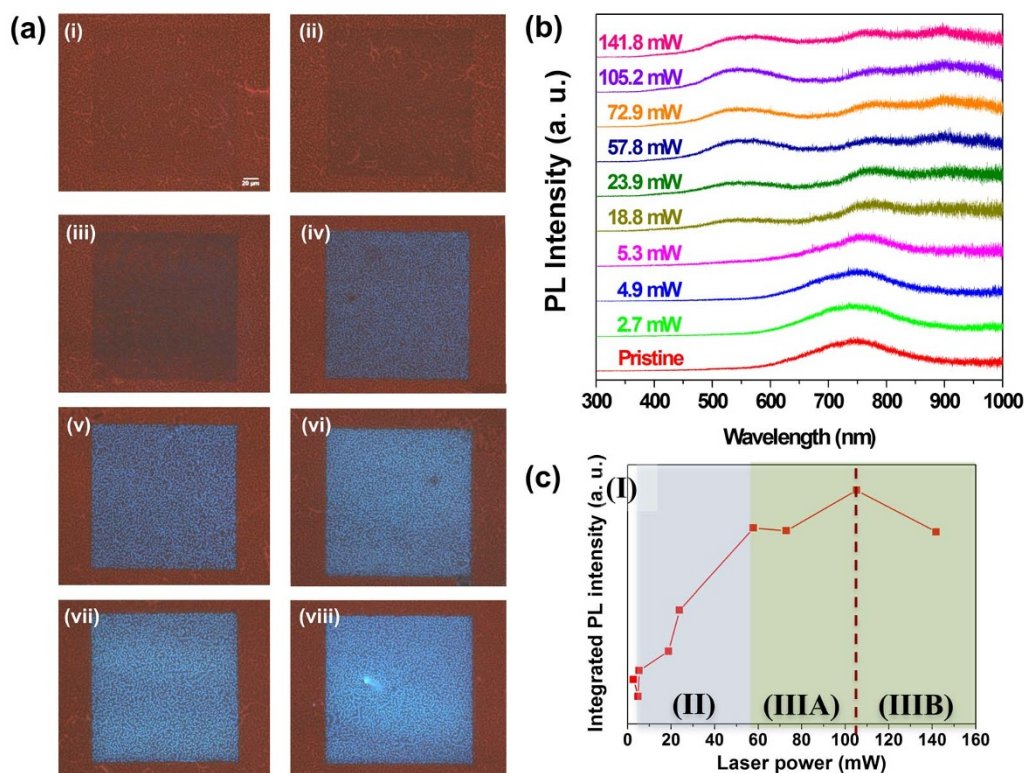


**Figure 3** | (a) FM images of microboxes created by focused laser scanning, with laser power of (i) 2.7 mW, (ii) 4.9 mW, (iii) 5.3 mW, (iv) 18.8 mW, (v) 23.9 mW, (vi) 57.8 mW, (vii) 72.9 mW and (viii) 105.2 mW. (b) PL spectra of the microboxes (i-viii) and that irradiated at 141.8 mW. (c) A plot of the integrated PL intensity (400 nm–600 nm) versus laser power, divided into the region I, II, IIIA and IIIB.



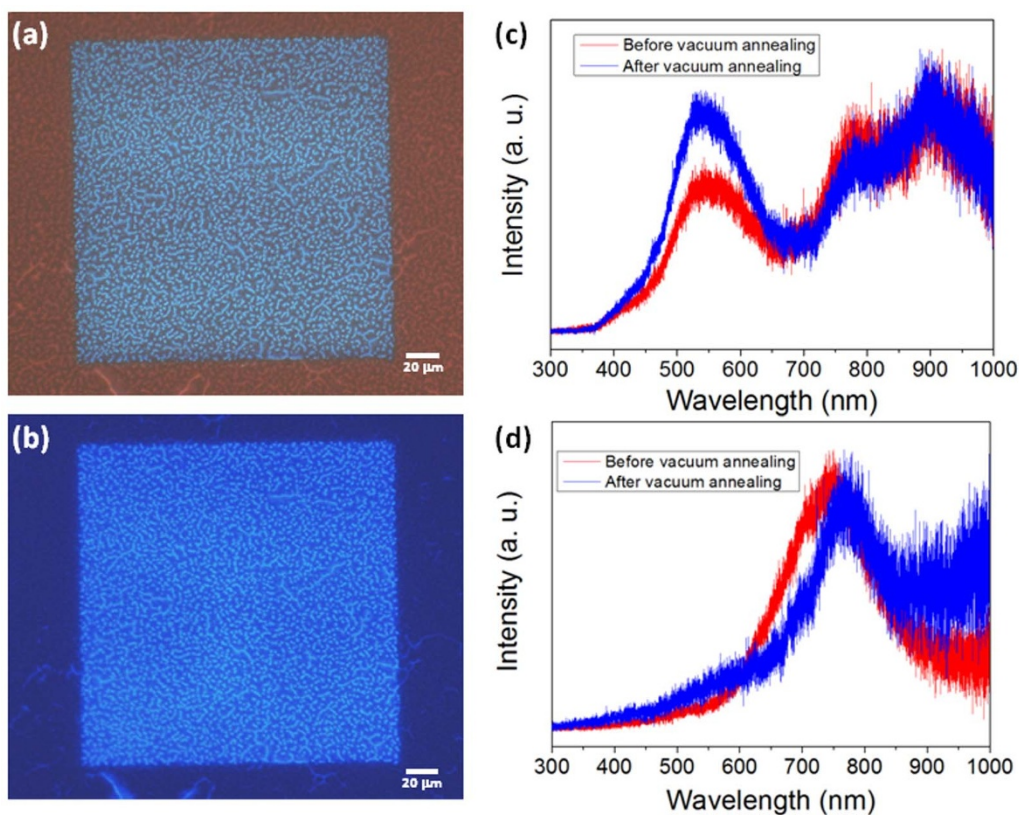


**Figure 4** | (a) A FM image of a micropattern created at a laser power of  $\sim 73$  mW. (b) A FM image of the micropattern (a) after 1-hr annealing in vacuum ( $10^{-2}$  Torr) at  $300^{\circ}\text{C}$ . (c) PL spectra of the laser-treated region before (in red) and after annealing (in blue). (d) PL spectra of the pristine mp-SiNWs before (in red) and after annealing (in blue).

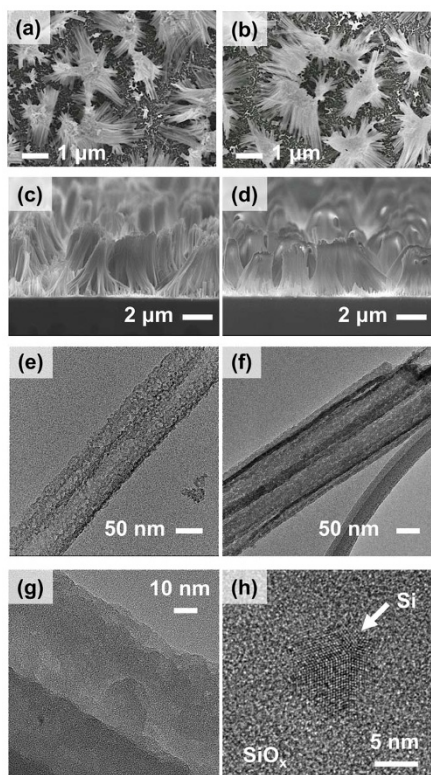


**Figure 5** | Morphology characterization of the pristine (a, c, e) and laser-modified (laser power of 55 mW) mp-SiNWs (b, d, f–h): (a, b) SEM top-down views; (c, d) SEM oblique views; (e–h) TEM images.

30.2%, increasing to 38.0% after laser irradiation at  $\sim 100$  mW. Secondly, it was reported that the transverse optical (TO)-phonon stretching mode of interfacial  $\text{Si-O}_x$  sensitively shifts with the sub-stoichiometry  $x$ :  $x=1.5$  at  $\sim 1050$   $\text{cm}^{-1}$ , and  $x=2$  at  $\sim 1078$   $\text{cm}^{-1}$ <sup>47</sup>. The pristine mp-SiNWs have the TO stretching at  $1068$   $\text{cm}^{-1}$ , illustrating  $1.5 < x < 2$  (Fig. 6). The laser modification at a power of  $\sim 73$  mW makes it shift to  $1076$   $\text{cm}^{-1}$ , illuminating the creation of nearly stoichiometric oxides owing to the laser-caused oxidation. Thirdly, bare Si wafers have a Raman vibration peak at  $523.1$   $\text{cm}^{-1}$ , attributed to the first-order TO-phonon mode of silicon (Fig. 7)<sup>48</sup>. The 1<sup>st</sup>-order TO-phonon mode downshifts to  $522.0$   $\text{cm}^{-1}$  in the as-grown mp-SiNWs, since the porosification of SiNWs substantially confines the phonon vibration in the shrinking silicon skeletons<sup>49,50</sup>. Laser irradiation causes a further downshift to  $521.0$   $\text{cm}^{-1}$ , illustrating that the laser-induced oxidation results in the shrinking of the porous Si skeletons to further confine the phonon vibration and reduce the porosity of mp-SiNWs (Fig. 5f vs 5e) to introduce tensile stress<sup>51</sup>. Fourthly, XPS shows that the as-grown mp-SiNWs present core  $\text{Si}_{2p}$  at  $99.5$  eV, and interfacial  $\text{Si}_{2p}\text{-O}$  at  $103.3$  eV owing to the natural oxidation (Fig. 8a(i)). Laser irradiation at  $\sim 90$  mW mostly eliminates the core  $\text{Si}_{2p}$  peak and enhances the  $\text{Si}_{2p}\text{-O}$  peak, as shown in Fig. 8a(ii). The laser-induced oxidation makes the interfacial  $\text{SiO}_x$  layer thicker, so that the  $\text{Si}_{2p}$  photoelectrons emitted from the underneath Si skeletons do not have sufficient energy to penetrate the thickening  $\text{SiO}_x$  layers, accounting for the disappearance of the core  $\text{Si}_{2p}$  peak. The laser-induced upshift of both  $\text{Si}_{2p}\text{-O}$  (Fig. 8a) and  $\text{O}_{1s}$  (Fig. 8b) towards higher binding energy indicates an increase of sub-stoichiometric  $x$  in  $\text{SiO}_x$ <sup>52</sup>.

To testify the effect of laser-induced oxidation, it was carried out rapid thermal annealing (RTA) of the pristine mp-SiNWs (supplementary information, Fig. S1–4). It was found that the reddish PL is eliminated by RTA at the annealing temperature over  $600^{\circ}\text{C}$ , but

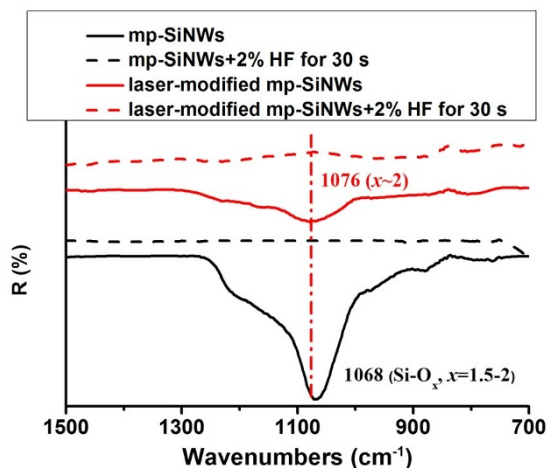


**Figure 6** | ATR-FTIR spectra of the pristine (in solid black) and laser-modified (in solid red) mp-SiNWs. Laser power was  $\sim 73$  mW. The pristine and laser-modified mp-SiNWs were etched in 2% HF for 30 s, in dash black and dash red, respectively.

there is no slight redshift of the reddish PL and generation of GB-PL. This could be ascribed to the fact that RTA is still very different from the laser treatment. Firstly, the heating and cooling rate of RTA is far slower than the laser scanning, and the cooling process in the laser modification is a very extreme quenching process. Secondly, RTA was carried out in a furnace to heat the air around the sample, whereas the laser only locally heats a small area of the sample as defined by the laser spot. Compared to the laser modification, the oxygen concentration will be highly reduced during the RTA-induced oxidation of the whole samples. This shows from another angle the uniqueness of laser modification in producing very bright GB-PL in a controlled pattern on mp-SiNWs.

**Proposed mechanisms.** Focused laser scanning oxidizes mp-SiNWs; hence it is natural to ask whether the GB-PL originates from the laser-induced oxidation. A micro-box was patterned at a power of  $\sim 70$  mW (Fig. 9a), and then immersed in 2% HF for 5 seconds. As a result, the reddish PL emitted from the pristine mp-SiNWs is nearly intact; however, the GB-PL completely vanishes (Fig. 9b). As characterized by ATR-FTIR, the TO-phonon mode of  $\text{SiO}_x$  in both pristine and laser-treated mp-SiNWs disappears after the HF treatment (the dashed lines in Fig. 6), indicating the removal of  $\text{SiO}_x$  by HF. As treated by HF, evidently the as-grown mp-SiNWs are intact but become more densely packed together, probably due to the capillary force during the drying process after the HF etching (Fig. 9c versus 9d). The laser-treated mp-SiNWs become withered after the HF etching, which is consistent with the laser-induced oxidation. The volume ratio of oxides increases under the laser-caused oxidation, so that the removal of  $\text{SiO}_x$  produces significant volume shrinkage in the laser-treated mp-SiNWs. The removal of  $\text{SiO}_x$  by HF eliminates the GB fluorescence, indicating the origin of GB-PL from the oxide-related species<sup>29</sup>, including  $\text{SiO}_x$ ,  $\text{O-h}^+$  (oxygen holes in the Si-O-Si bridging structures), and local oxide defects<sup>23,24,53</sup>. Oxide defects may stem from the rapid annealing/quenching process by rapidly scanning the high-power focused laser beam on the samples.

The laser-induced oxidation creates nearly-stoichiometric  $\text{SiO}_2$  oxides (Fig. 6), which has a band gap larger than 8 eV<sup>24</sup>. The PL excitation energy ( $\lambda = 325$  nm, i.e. 3.8 eV) is far below the oxide band gap, so as to exclude the contribution from the oxides. To further explore the GB-PL mechanism, the laser modification as function of laser power (i.e. Fig. 3) was characterized by Raman scattering in Fig. 10a. It should be emphasized that the penetration depth in Si is  $\sim 300$  nm at Raman excitation  $\lambda$  of 532 nm<sup>54</sup>, only one tenth of the length of mp-SiNWs. Although there are voids in the array of mp-

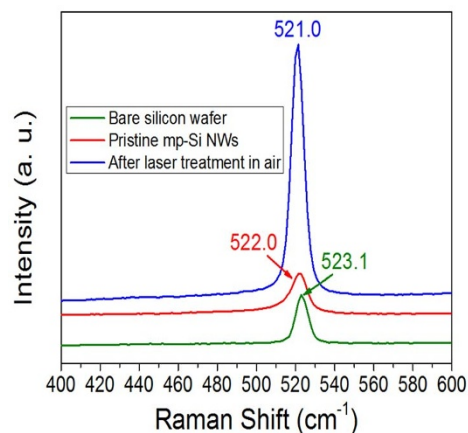


**Figure 7** | Raman spectra of bare Si wafer (in green), the pristine mp-SiNWs (in red) and laser-modified mp-SiNWs (in blue). Laser power was  $\sim 73$  mW.

SiNWs on a Si wafer, the Raman vibrations detected in Fig. 10a mainly stem from the thick layer of mp-SiNWs instead of the underneath wafer. The 1<sup>st</sup>-order TO-phonon mode of Si varies with the laser power, with respect to the peak shape and position. The TO-mode is modeled by the Fano line shape, given by<sup>55</sup>

$$I(\omega) = A \frac{(q + \varepsilon)^2}{(1 + \varepsilon^2)} \quad (1)$$

$$\varepsilon = \frac{(\omega - \omega_0)}{\Gamma} \quad (2)$$

where  $I$  is Raman scattering intensity,  $\omega$  is Raman shift,  $\omega_0$  is the TO-mode peak position, and  $A$  is a pre-constant.  $q$  is the asymmetry parameter, and  $1/q$  represents the coupling strength.  $\Gamma$  is the line-width, and  $1/\Gamma$  represents the phonon lifetime. The Fano-fitting results are summarized in Fig. 10b, in terms of  $\omega_0$ ,  $1/q$  and  $1/\Gamma$ . It is illuminated in Fig. 3 and Fig. 10b that there are three regions (I-III) defined by two transition points, i.e.  $\sim 5$  mW and  $\sim 55$  mW. The first transition point is the threshold to excite GB-PL (Fig. 3a), and the second is the threshold to cause a significant change in the three Fano parameters (Fig. 10b). Herein, the power range of  $< 5$  mW, 5–55 mW and  $> 55$  mW are denoted as the region I, II and III, respectively. The as-grown mp-SiNWs emit the reddish PL in the region I, and the emission turns to be GB dominantly in the region II–III. In the region III,  $\omega_0$  and  $(1/q)$  have a monolithic change with laser power, but  $(1/\Gamma)$  reaches its maximum at  $\sim 105$  mW. So the region III is further differentiated as the region IIIA (55–105 mW) and IIIB ( $> 105$  mW). The downshift of  $\omega_0$  in the region III is attributed to that laser irradiation oxidizes mp-SiNWs to confine the phonon vibrations of Si skeletons. As comparison  $\omega_0$  barely alters in the region II, indicating no oxidation due to relatively low laser power less than 55 mW. Above 55 mW, the laser scanning effectively triggers the oxidation of mp-SiNWs, leading to the creation of  $\text{O-h}^+$  and oxide defects in the thickening  $\text{SiO}_x$  layers covering the Si skeletons. The coupling ( $1/q$ ) refers to the interference of Si phonons with the interfacial states (i.e. oxide defects and/or  $\text{O-h}^+$ ), and the monolithic increase of  $(1/q)$  in the region III is ascribed to the increasing amount of the interfacial states. Fig. 6 illuminates the stoichiometric oxidation (i.e.  $\text{SiO}_2$ ) is nearly achieved at 73 mW, as marked by a dash black circle in Fig. 10b. Above 73 mW, the stoichiometric oxidation can significantly diminish the interfacial concentration of  $\text{O-h}^+$ , but continuously increase that of oxide defects due to the faster heating/quenching processes at high laser power. It is notable that phonon lifetime ( $1/\Gamma$ ) is elongated in the region IIIA due to the constructive interference, and reduced in the region IIIB owing to the destructive



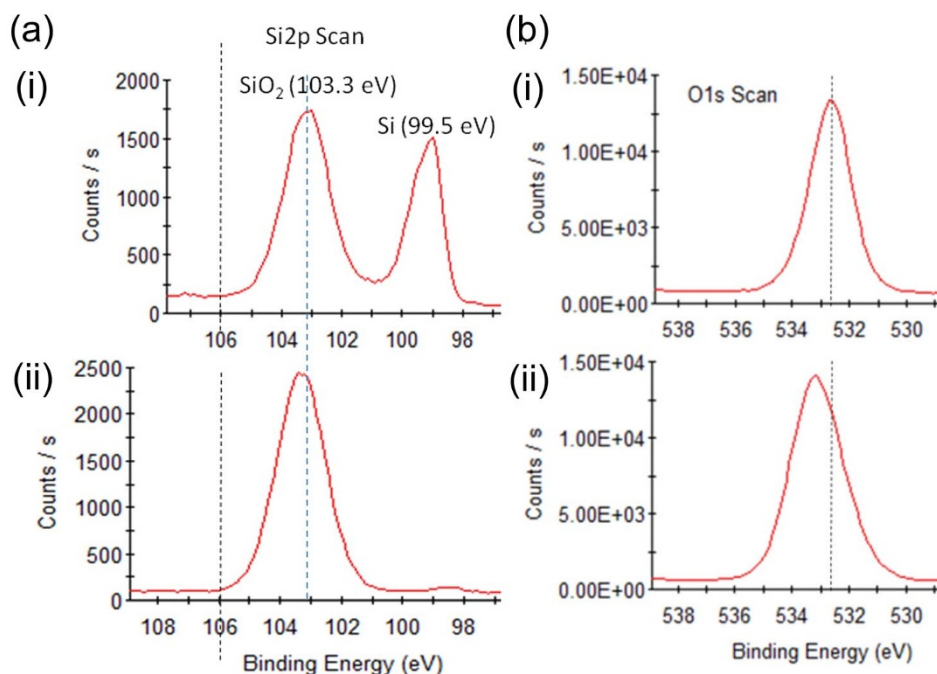


**Figure 8** | XPS spectra of the as-grown (i) and laser-modified (ii) mp-SiNWs: (a) Si2p, and (b) O1s. Laser power was  $\sim 90$  mW.

interference. The phonons couple to  $O-h^+$  constructively but to oxide defects destructively, accounting for the non-monolithic change of  $(I/I)$  in the region III. With increasing laser power, the destructive interference of oxide defects tends to overbalance the constructive interference of  $O-h^+$ . As a result,  $(I/I)$  reaches its maximum at 105 mW, beyond which the destructive interference dominates to deteriorate the phonon lifetime in the region IIIB. Both constructive and destructive coupling contribute to enhancing the

interference strength  $(1/q)$ , leading to a monolithic increase with laser power in the region III. Note that the discussion in Figs. 4–9 refers to the region IIIA. In the region II, the lack of laser-induced oxidation causes little change in either  $(1/q)$  or  $(I/I)$ .

Accordingly, a GB-PL mechanism is proposed in Fig. 11 with respect to the power-dependent region I–III. To generate the GB-PL, electrons are excited to a PL excitation state, non-irradiatively relax to the GB band (1.9–2.5 eV above the VB-valence band of  $SiO_x$ , as marked by an orange band), irradiatively transit to VB and then emit the GB-PL. From the energy point of view, it is prerequisite that there is energy state within the GB band. Furthermore, if electrons were excited to a virtual excitation state, the possibility to generate the GB-PL would be greatly reduced. In this work, the PL excitation has an energy of 3.8 eV, too low to excite electrons over the band gap of  $SiO_x$  ( $1.5 < x < 2$ ) in the as-grown mp-SiNWs. Consequently, it is proposed there is no density of states in either the GB band or PL excitation state to account for the lack of GB-PL in the pristine mp-SiNWs or the region I, even though there may be a few surface states out of the GB band. In the region II, although without laser-induced oxidation, the quick melting/re-solidification induced by the fast laser scanning most likely affects the surfaces of mp-SiNWs and creates some surface states in the GB band (Fig. 11-II), leading to the generation of GB-PL having an intensity increasing with laser power (Fig. 3c-II). The focused laser commences to oxidize mp-SiNWs at 55 mW, and creates oxide defects and  $O-h^+$  leading to an increase in density of states in the GB band and/or the PL excitation state (Fig. 11-IIIa). It accounts for the continuous enhancement in the GB-PL intensity with laser power. In the region IIIB, the interfacial concentration of oxide defects increases with laser power, accompanied with the reduce in that of  $O-h^+$ . Given that  $O-h^+$  has density of states in the GB band as proposed in the IIIa, the reduce of  $O-h^+$  gives rise to a decrease of density of states in the GB band. With an increase of laser power, the laser-induced oxidation becomes stoichiometric, resulting in an energy upshift of the interfacial oxide layers. The emerging oxide defects in the layers increase density of states above the GB band. As a net result, density of states in the GB band tend to reduce (Fig. 11-IIIb), resulting in an unexpected reduction in the GB-PL intensity. As derived from the experimental data,

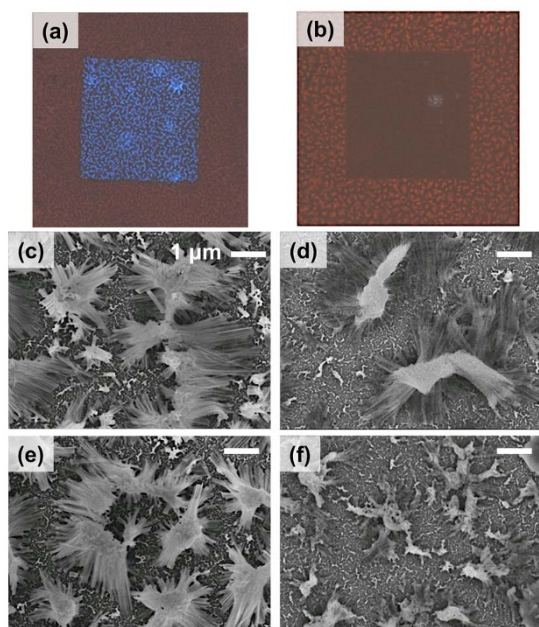


**Figure 9** | FM images of mp-SiNWs before (a) and after (b) 2% HF etching for 5 s. The middle micro-box in (a) and (b) was the area exposed to the focused laser irradiation at  $\sim 70$  mW. SEM top-down views of as-grown mp-SiNWs before (c) and after (d) HF etching, and laser-modified mp-SiNWs before (e) and after (f) HF etching. Note that the scale bars in (c–f) all represent 1  $\mu$ m.

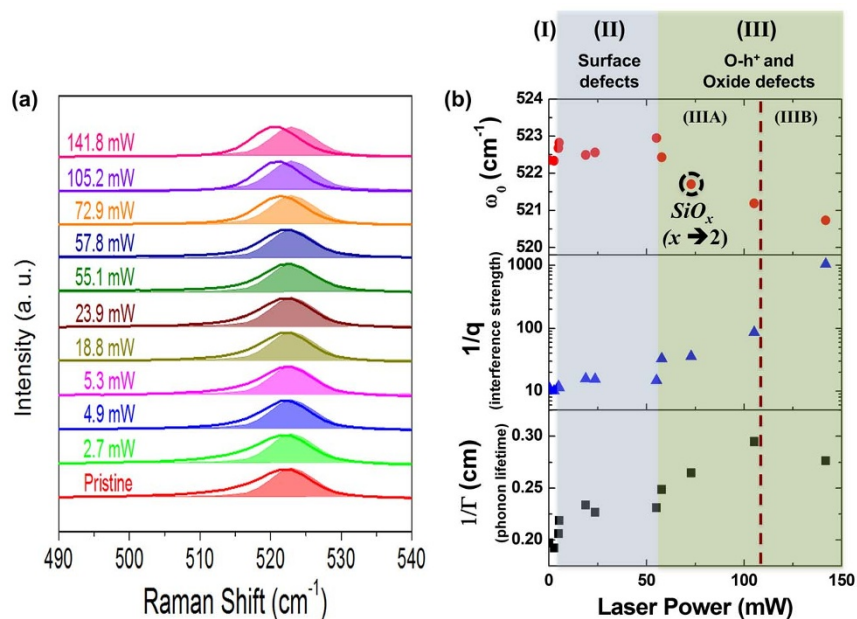


**Figure 10** | (a) Raman spectra of mp-SiNWs modified by focused laser beam with laser power in a range of 0–142 mW, as shown in Fig. 3. For comparison, the Raman spectrum of a bare Si wafer was added as the color-filled peak in each spectrum. (b) The Fano line shape fitting to the Raman spectra of (a), using eq. 1–2. The dash black circle indicates the nearly-stoichiometric laser-induced oxidation at a laser power of 73 mW. The plot is divided into the regions as same as Fig. 3c.

the proposed laser-modification mechanism need to be further verified by more advanced surface-characterization techniques.

The proposed mechanism can account for the annealing effect, as shown in Fig. 4. The annealing at  $10^{-2}$  Torr and  $300^{\circ}\text{C}$  leads to mild oxidation of both pristine and laser-modified mp-SiNWs. As a result, the laser-modified mp-SiNWs emit the GB-PL with enhanced intensity (Fig. 4c), and a weak GB-PL was detected in the as-grown mp-SiNWs (Fig. 4d). After the in-vacuum annealing, the reddish PL of the pristine mp-SiNWs tends to redshift toward the near infrared region (Fig. 4d), making the reddish PL fade. The generation of weak GB-PL and the fading of the reddish PL make the as-grown mp-

SiNWs appear to have blue fluorescence after the in-vacuum annealing, as shown in Fig. 4b.

It is shown in Fig. 2c and 3b that focused laser scanning effectively suppresses the reddish PL of the as-grown mp-SiNWs and makes it redshift. If the reddish PL originated from QC of the Si skeletons, the laser-induced oxidation shrinks the Si skeletons and should make it blueshift. So it is highly probable that the reddish PL stems from the defects at the  $\text{SiO}_x/\text{Si}$  interfaces<sup>21</sup>. The laser-induced oxidation alters the nature of the interfacial defects, accounting for the redshift. Under the PL excitation, there may be a competition in the optical absorption between the laser-induced oxide states and the interfacial

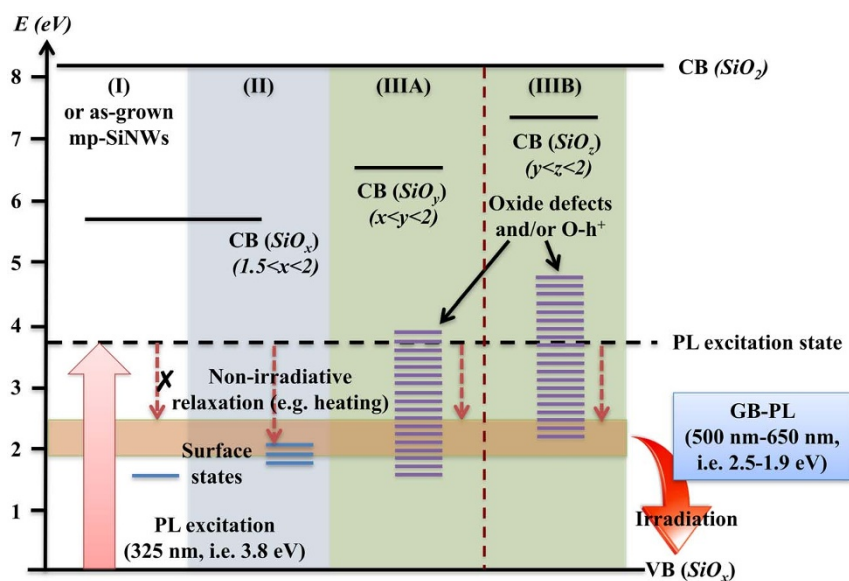


**Figure 11** | Schematic energy diagram to account for the laser-induced emission of greenish-blue (GB) PL. “VB” and “CB” are denoted as valence and conduction band, respectively. The set of CB of non-stoichiometric oxides are arbitrarily positioned between the CB of  $\text{SiO}_2$  and PL excitation state. The orange energy band is the GB band, and the irradiation transition from the GB band to VB creates the GB-PL. The laser-induced regions (I–IIIB) are referred to those in Fig. 3c and Fig. 10b.





defects. The GB-PL deteriorates the reddish PL, probably because the absorption cross-section of the laser-induced states overbalances that of the interfacial defects. Another exploration is that the incoming photons induce the interband absorption in the interfacial defects, and then the energy transfers to the laser-induced oxide states.

**A prospective application in creating hidden images.** Once establishing the control over the optical properties of mp-SiNWs by the focused laser scanning, we could engineer functional components with interesting applications, e.g. creation of hidden images as shown in Fig. 12. Firstly, the boundary of a box was created at a laser power of 92 mW, which is visible under the bright field optical microscopy (Fig. 12a and 12c). Then reduce the laser power to  $\sim 18$  mW to create two different micropatterns within the boxes. The laser power is too low to make the micropatterns visible under the bright field optical microscopy. However, the hidden micropatterns were revealed very readily under FM (Fig. 12b and 12d), demonstrating the feasibility of the creation of hidden images.

## Conclusions

MACE was carried out to generate mp-SiNWs emitting the reddish PL, ascribed to the porosification-generated defects at the  $\text{SiO}_x/\text{Si}$  interfaces. Fast scanning mp-SiNWs by a focused green laser (532 nm) generates the GB-PL together with the significant quenching and slight redshift of the reddish PL. With respect to the laser power, the laser modification is divided into three regions: 0–5 mW (the region I), 5–55 mW (the region II),  $>55$  mW (the region III). The threshold to generate the GB-PL is  $\sim 5$  mW, and the laser modification is negligible in the region I. In the region II, the fast scanning with relatively low laser power gives rise to quick melting/re-solidification on the surfaces of mp-SiNWs, and consequently creates surface states in the GB band to facilitate the emission of the GB-PL. In the region III, the laser scanning with high laser power effectively oxidizes mp-SiNWs, as fully confirmed by EDS, ATR-FTIR, Raman scattering and XPS. The laser-induced oxidation substantially thickens the interfacial  $\text{SiO}_x$  layers with an increase of  $x$  towards 2, and creates oxide defects and  $\text{O-h}^+$  in the oxide layers.  $\text{O-h}^+$  constructively couples with Si phonons to elongate the phonon lifetime; on the contrary, the phonon lifetime is reduced by the destructive interference of oxide defects. At a laser power above  $\sim 70$  mW,

the laser-induced oxide layers turn to be stoichiometric, leading to a diminishment in the interfacial concentration of  $\text{O-h}^+$ . Meanwhile, the quick heating/quenching process at high laser power effectively increases the amount of oxide defects. The destructive interference of oxide defects becomes dominant at  $>105$  mW, so the region III can be further divided into IIIA (55–105 mW) and IIIB ( $>105$  mW). In the region IIIA, the laser-induced generation of oxide defects and  $\text{O-h}^+$  effectively increases density of states in the GB band and PL excitation state, resulting in the magnification of the GB-PL intensity with laser power. In the region IIIB, however, the further generation of oxide defects magnifies density of states above the GB band and the diminishment of  $\text{O-h}^+$  reduces density of states in the GB band, accounting for the quenching of GB-PL. In addition, the in-vacuum annealing can effectively enhance the GB-PL in both the pristine and laser-modified mp-SiNWs. It is demonstrated that the micropatterns created at a low laser power (e.g.  $<20$  mW) are invisible under the bright-field optical microscope but become apparent under fluorescence microscope, indicating the feasibility in the creation of hidden images.

## Methods

**Fabrication of mp-SiNWs.** mp-SiNWs were fabricated by MACE of n-Si(100) (doped with As, electrical resistivity of 1–5  $\text{m}\Omega\cdot\text{cm}$ , Semiconductor Wafer, Inc.). The wafers ( $1.5 \times 1.5 \text{ cm}^2$ ) were subsequently degreased in acetone, ethanol and Piranha (98%  $\text{H}_2\text{SO}_4/30\% \text{H}_2\text{O}_2=3/1$ , v/v) at room temperature, and dipped in 5% HF for 15 min to completely remove native oxides. Then the treated wafers were transferred into a Teflon beaker, which held an aqueous solution containing 2.4 mol/L HF and 0.02 mol/L  $\text{AgNO}_3$  to carry out MACE. A piece of aluminum foil shielded the beaker from solar illumination in order to uniformly create SiNWs on the whole wafers, and the etching was ambiently operated without control over temperature. It took 1 hour in MACE to create mp-SiNWs as long as roughly 3.5  $\mu\text{m}$ . When the etching was over, the wafers were covered with a thick layer of Ag dendrites, which was dissolved in 68%  $\text{HNO}_3$  immediately.

**Focused Laser Beam micropatterning.** The focused laser beam system comprised of a simple upright optical microscope that was coupled with an external laser beam (Fig. 1). A SUWTECH LDC-2500 diode laser ( $\lambda = 532 \text{ nm}$ , maximum power  $\sim 300 \text{ mW}$ ) was used, and the parallel emitted laser beam was directed into the upright optical microscope via two reflecting mirrors (M1 and M2). Inside the microscope, the beam was directed towards an objective lens (L) via a dichroic filter (DC). The laser beam was then focused by the objective lens with a magnification of 50 $\times$ , a numerical aperture of 0.55 and a long working distance of 8.7 mm. Beam waist of the focused laser, i.e. the spot size, was  $\sim 4 \mu\text{m}$ . The power of the laser beam focused onto a sample was measured at the position between the objective lens and sample. The samples were placed on a computer-controlled, motorized stage (MICOS VT-80 System) with a minimum step size of 100 nm in the x–y plane. By moving the sample stage in a programmable manner with respect to the focused beam, we were able to create a wide variety of micropatterns on substrates. During the laser beam modification process, the scanning speed was 50  $\mu\text{m/s}$ . The same objective lens (L) was used to collect light reflected from the sample for viewing purposes. A CCD camera was used to capture the images of the laser trimming process, hence we could visually inspect the structures created simultaneously through a TV monitor.

**Morphology Characterization.** Si wafers with pristine or laser-modified mp-SiNWs were mechanically split, leaving the freshly split cross sections to study morphology by field emission scanning electron microscopy (FESEM, JEOL JSM-6700F). The chemical composition was analyzed by energy-dispersive X-ray spectroscopy (EDS, equipped with FESEM). For transmission electron microscopy (TEM, Tecnai G2 20 S-TWIN, HKBU) analyses, mp-SiNWs were scratched off from the wafers and transferred to isopropanol. After 5-min sonication to well disperse mp-SiNWs in isopropanol, several drops of the mixture were applied to a lacey carbon film on a grid structure (Electron Microscopy Sciences). The grid was dried and then inspected by TEM.

**Spectral Characterization.** Si wafers with pristine or laser-modified mp-SiNWs were directly characterized by diverse spectral techniques. Fluorescence microscopy (FM) was carried out with a Olympus BX51 Fluorescence Upright Microscope, and a mercury light source system (U-HGLGPS light source) serves as the fluorescence light source. The Olympus BX51 was fitted with a few fluorescence mirror units. In this work, all the FM images presented were obtained when the mp-SiNW arrays were subjected to the UV excitation whereby fluorescence mirror unit with a wide UV excitation band of 330–385 nm was utilized. X-ray photoelectron spectroscopy (XPS) was carried out using a VG ESCALAB 200i-XL X-ray photoelectron spectroscopy system. A monochromatic  $\text{Al K}\alpha$  (1486.6 eV) X-ray with a diameter of 700  $\mu\text{m}$  was employed while the photoelectrons were collected at a normal take-off angle (with respect to surface plane). C1s peak from adventitious carbon at 285.0 eV is used as a reference for charge correction. Photoluminescence microscopy was carried out using

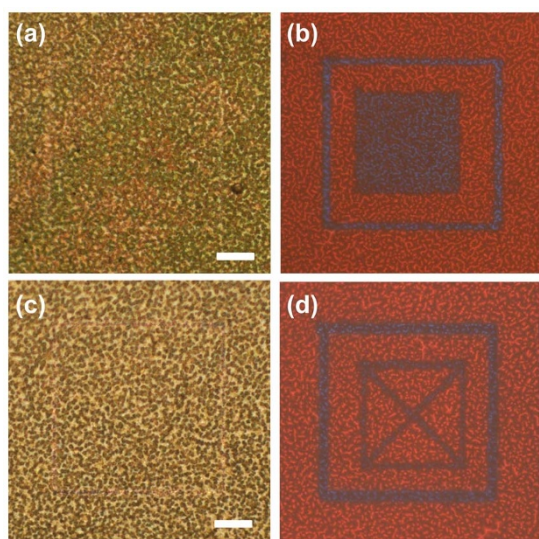


**Figure 12** | mp-SiNW arrays were scanned by focused laser beam in two different patterns, imaged by bright-field optical microscope (a, c) and FM (b, d). Two microscopies image the same sample: (a) versus (b), and (c) versus (d).





a Renishaw inVia system with a Kimmon 1K Series He-Cd laser with a wavelength of 325 nm which was focused by a 40X UV objective lens onto the mp-SiNW arrays. The room-temperature micro-photoluminescence (Renishaw inVia) were collected in a backscattering geometry. Micro-Raman measurements were carried out via the same setup, except for the excitation by a 532 nm laser focused onto the mp-SiNW arrays with a 50X objective lens. ATR-FTIR (PerkinElmer Spectrum Two, with a Horizontal ATR accessory from PIKE Technologies, germanium crystal, DTGS detector) was operated at an incident angle of 45°.

- Rong, H. S. *et al.* An all-silicon Raman laser. *Nature* **433**, 292–294 (2005).
- Boyras, O. & Jalali, B. Demonstration of a silicon Raman laser. *Opt. Express* **12**, 5269–5273 (2004).
- Yan, R. X. *et al.* Nanowire-based single-cell endoscopy. *Nat. Nanotechnol.* **7**, 191–196 (2012).
- Coe, S., Woo, W. K., Bawendi, M. & Bulovic, V. Electroluminescence from single monolayers of nanocrystals in molecular organic devices. *Nature* **420**, 800–803 (2002).
- Cloutier, S. G., Kossyrev, P. A. & Xu, J. Optical gain and stimulated emission in periodic nanopatterned crystalline silicon. *Nat. Mater.* **4**, 887–891 (2005).
- Schaller, R. D., Agranovich, V. M. & Klimov, V. I. High-efficiency carrier multiplication through direct photogeneration of multi-excitons via virtual single-exciton states. *Nat. Phys.* **1**, 189–194 (2005).
- Timmerman, D., Izeddin, I., Stallinga, P., Yassievich, I. N. & Gregorkiewicz, T. Space-separated quantum cutting with silicon nanocrystals for photovoltaic applications. *Nat. Photonics* **2**, 105–109 (2008).
- Shabaev, A., Efros, A. L. & Nozik, A. J. Multiexciton generation by a single photon in nanocrystals. *Nano Lett.* **6**, 2856–2863 (2006).
- Tian, B. Z. *et al.* Coaxial silicon nanowires as solar cells and nanoelectronic power sources. *Nature* **449**, 885–889 (2007).
- Park, J. H. *et al.* Biodegradable luminescent porous silicon nanoparticles for in vivo applications. *Nat. Mater.* **8**, 331–336 (2009).
- Kovalev, D., Heckler, H., Polisski, G. & Koch, F. Optical properties of Si nanocrystals. *Phys. Status Solidi B-Basic Res.* **215**, 871–932 (1999).
- de Boer, W. *et al.* Red spectral shift and enhanced quantum efficiency in phonon-free photoluminescence from silicon nanocrystals. *Nat. Nanotechnol.* **5**, 878–884 (2010).
- Kang, Z. H. *et al.* A polyoxometalate-assisted electrochemical method for silicon nanostructures preparation: From quantum dots to nanowires. *J. Am. Chem. Soc.* **129**, 5326–5327 (2007).
- Lu, Z. H., Lockwood, D. J. & Baribeau, J. M. Quantum Confinement and Light-Emission in SiO<sub>2</sub>/Si Superlattices. *Nature* **378**, 258–260 (1995).
- Pavesi, L., Dal Negro, L., Mazzoleni, C., Franzo, G. & Priolo, F. Optical gain in silicon nanocrystals. *Nature* **408**, 440–444 (2000).
- Kang, Z. H. *et al.* Water-Soluble Silicon Quantum Dots with Wavelength-Tunable Photoluminescence. *Adv. Mater.* **21**, 661–664 (2009).
- Gupta, A., Swihart, M. T. & Wiggers, H. Luminescent Colloidal Dispersion of Silicon Quantum Dots from Microwave Plasma Synthesis: Exploring the Photoluminescence Behavior Across the Visible Spectrum. *Adv. Funct. Mater.* **19**, 696–703 (2009).
- Canham, L. T., Houlton, M. R., Leong, W. Y., Pickering, C. & Keen, J. M. Atmospheric Impregnation of Porous Silicon At Room-Temperature. *J. Appl. Phys.* **70**, 422–431 (1991).
- Peng, K. Q., Yan, Y. J., Gao, S. P. & Zhu, J. Synthesis of large-area silicon nanowire arrays via self-assembling nanoelectrochemistry. *Adv. Mater.* **14**, 1164–1167 (2002).
- Qu, Y. Q. *et al.* Electrically Conductive and Optically Active Porous Silicon Nanowires. *Nano Lett.* **9**, 4539–4543 (2009).
- Hochbaum, A. I., Gargas, D., Hwang, Y. J. & Yang, P. D. Single Crystalline Mesoporous Silicon Nanowires. *Nano Lett.* **9**, 3550–3554 (2009).
- Canham, L. T. Silicon Quantum Wire Array Fabrication By Electrochemical And Chemical Dissolution Of Wafers. *Appl. Phys. Lett.* **57**, 1046–1048 (1990).
- Lin, J., Zhang, L. Z., Zhang, B. R., Zong, B. Q. & Qin, G. G. Stable Blue-Light Emission From Oxidized Porous Silicon. *J. Phys.-Condensed Matter* **6**, 565–568 (1994).
- Tsybeskov, L., Vandyshev, J. V. & Fauchet, P. M. Blue Emission In Porous Silicon - Oxygen-Related Photoluminescence. *Phys. Rev. B* **49**, 7821–7824 (1994).
- Anedda, A. *et al.* A 1.9 eV Photoluminescence Induced By 4 eV Photons In High-Purity Wet Synthetic Silica. *J. Appl. Phys.* **74**, 6993–6995 (1993).
- Petrovakocho, V., Muschik, T., Kovalev, D. I., Koch, F. & Lehmann, V. *Fast photoluminescence from porous silicon. 1992 MRS Fall Meeting: Microcrystalline Semiconductors: Materials Science & Devices, Boston. Pittsburgh: Materials Research Soc.* (1992, Nov 30–Dec 4).
- Tsai, C. *et al.* Thermal-Treatment Studies of The Photoluminescence Intensity of Porous Silicon. *Appl. Phys. Lett.* **59**, 2814–2816 (1991).
- Perez, J. M. *et al.* Direct Evidence For The Amorphous-Silicon Phase In Visible Photoluminescent Porous Silicon. *Appl. Phys. Lett.* **61**, 563–565 (1992).
- Cullis, A. G., Canham, L. T. & Calcott, P. D. J. The structural and luminescence properties of porous silicon. *J. Appl. Phys.* **82**, 909–965 (1997).
- Mauckner, G. *et al.* Origin of the infrared band from porous silicon. 1994 MRS Fall Meeting: Microcrystalline and Nanocrystalline Semiconductors, Boston. Pittsburgh: Materials Research Soc. (1994, Nov 28–Dec 2).
- Koch, F. *Models and mechanisms for the luminescence of porous Si. 1993 MRS Spring Meeting: Silicon-Based Optoelectronic Materials, San Francisco. Pittsburgh: Materials Research Soc.* (1993, Apr 12–16).
- Fauchet, P. M. *et al.* Can Oxidation And Other Treatments Help Us Understand The Nature Of Light-Emitting Porous Silicon? 1993 MRS Spring Meeting: Silicon-Based Optoelectronic Materials, San Francisco. Pittsburgh: Materials Research Soc. (1993, Apr 12–16).
- Ghoshal, S. K., Mohan, D., Kassa, T. T. & Sharma, S. Nanosilicon for photonic applications. *Int. J. Mod. Phys. B* **21**, 3783–3796 (2007).
- To, W. K., Fu, J. X., Yang, X. B., Roy, V. A. L. & Huang, Z. F. Porosification-reduced optical trapping of silicon nanostructures. *Nanoscale* **4**, 5835–5839 (2012).
- Jia, H. P. *et al.* Novel Three-Dimensional Mesoporous Silicon for High Power Lithium-Ion Battery Anode Material. *Adv. Energy Mater.* **1**, 1036–1039 (2011).
- Wang, X. L. & Han, W. Q. Graphene Enhances Li Storage Capacity of Porous Single-Crystalline Silicon Nanowires. *ACS Appl. Mater. Interfaces* **2**, 3709–3713 (2010).
- Qu, Y. Q. *et al.* Photocatalytic properties of porous silicon nanowires. *J. Mater. Chem.* **20**, 3590–3594 (2010).
- Xue, M. *et al.* pH-Operated Mechanized Porous Silicon Nanoparticles. *J. Am. Chem. Soc.* **133**, 8798–8801 (2011).
- Peng, K. Q., Wang, X. & Lee, S. T. Gas sensing properties of single crystalline porous silicon nanowires. *Appl. Phys. Lett.* **95**, 243112 (2009).
- Chiappini, C., Liu, X. W., Fakhoury, J. R. & Ferrari, M. Biodegradable Porous Silicon Barcode Nanowires with Defined Geometry. *Adv. Funct. Mater.* **20**, 2231–2239 (2010).
- He, H. P., Liu, C., Sun, L. W. & Ye, Z. Z. Temperature-dependent photoluminescence properties of porous silicon nanowire arrays. *Appl. Phys. Lett.* **99**, 123106 (2011).
- To, W. K., Tsang, C. H., Li, H. H. & Huang, Z. F. Fabrication of n-Type Mesoporous Silicon Nanowires by One-Step Etching. *Nano Lett.* **11**, 5252–5258 (2011).
- Chen, H. H. *et al.* Lightly doped single crystalline porous Si nanowires with improved optical and electrical properties. *J. Mater. Chem.* **21**, 801–805 (2011).
- Lettieri, S., Maddalena, P., Di Francia, G. & Morvillo, P. Influence of doping concentration on the photoluminescence of silicon nanocrystals. *Phys. Status Solidi A-App. Res.* **197**, 399–402 (2003).
- Lin, L. H., Guo, S. P., Sun, X. Z., Feng, J. Y. & Wang, Y. Synthesis and Photoluminescence Properties of Porous Silicon Nanowire Arrays. *Nanoscale Res. Lett.* **5**, 1822–1828 (2010).
- Lin, L. H. *et al.* Photoluminescence origins of the porous silicon nanowire arrays. *J. Appl. Phys.* **110**, 073109 (2011).
- Lambers, J. & Hess, P. Infrared spectra of photochemically grown suboxides at the Si/SiO<sub>2</sub> interface. *J. Appl. Phys.* **94**, 2937–2941 (2003).
- Adu, K. W., Xiong, Q., Gutierrez, H. R., Chen, G. & Eklund, P. C. Raman scattering as a probe of phonon confinement and surface optical modes in semiconducting nanowires. *Appl. Phys. A* **85**, 287–297 (2006).
- Campbell, I. H. & Fauchet, P. M. The effects of microcrystal size and shape on the one phonon Raman spectra of crystalline semiconductors. *Solid State Commun.* **58**, 739–741 (1986).
- Kanemitsu, Y. *et al.* Microstructure and optical properties of free-standing porous silicon films: Size dependence of absorption spectra in Si nanometer-sized crystallites. *Phys. Rev. B* **48**, 2827–2830 (1993).
- Khriachtchev, L., Rasanen, M. & Novikov, S. Laser-controlled stress of Si nanocrystals in a free-standing Si/SiO<sub>2</sub> superlattice. *Appl. Phys. Lett.* **88**, 013102 (2006).
- Ishizaka, A., Iwata, S. & Kamigaki, Y. Si-SiO<sub>2</sub> interface characterization by ESCA. *Surf. Sci.* **84**, 355–374 (1979).
- Rehm, J. M., McLendon, G. L., Tsybeskov, L. & Fauchet, P. M. How methanol affects the surface of blue and red emitting porous silicon. *Appl. Phys. Lett.* **66**, 3669–3671 (1995).
- Song, J. J. *et al.* Penetration depth at various Raman excitation wavelengths and stress model for Raman spectrum in biaxially-strained Si. *Sci. China-Phys. Mech. Astron.* **56**, 2065–2070 (2013).
- Gupta, R., Xiong, Q., Adu, C. K., Kim, U. J. & Eklund, P. C. Laser-induced Fano resonance scattering in silicon nanowires. *Nano Lett.* **3**, 627–631 (2003).

## Acknowledgments

The authors thank Dr. Sara Azimi (NUS) in the HF etching, and Mr. Benson Siu-Cheong Leung (Physics, HKBU) in the TEM characterization (funded by SEG\_HKBU06), and acknowledge the financial support of Faculty of Science at HKBU, the NUS and NUS International Collaboration Fund.

## Author contributions

Y.R., M.R. and F. carried out the experimental work and analyzed the data, J.J. fabricated mp-SiNWs, E.S. operated XPS and analyzed the XPS data, Z.F. and C.H. supervised the experimental work, analyzed the data and wrote the main manuscript text. Y.R., M.R. and F. contributed equally to this work.



## Additional information

Supplementary information accompanies this paper at <http://www.nature.com/scientificreports>

**Competing financial interests:** The authors declare no competing financial interests.

**How to cite this article:** Choi, Y.-R. *et al.* Laser-induced Greenish-Blue Photoluminescence of Mesoporous Silicon Nanowires. *Sci. Rep.* 4, 4940; DOI:10.1038/srep04940 (2014).



This work is licensed under a Creative Commons Attribution-NonCommercial-NoDerivs 3.0 Unported License. The images in this article are included in the article's Creative Commons license, unless indicated otherwise in the image credit; if the image is not included under the Creative Commons license, users will need to obtain permission from the license holder in order to reproduce the image. To view a copy of this license, visit <http://creativecommons.org/licenses/by-nc-nd/3.0/>